Joule

CellPress
OPEN ACCESS

Article

Low-cost photoreactors for highly photon/energy-efficient solar-driven synthesis

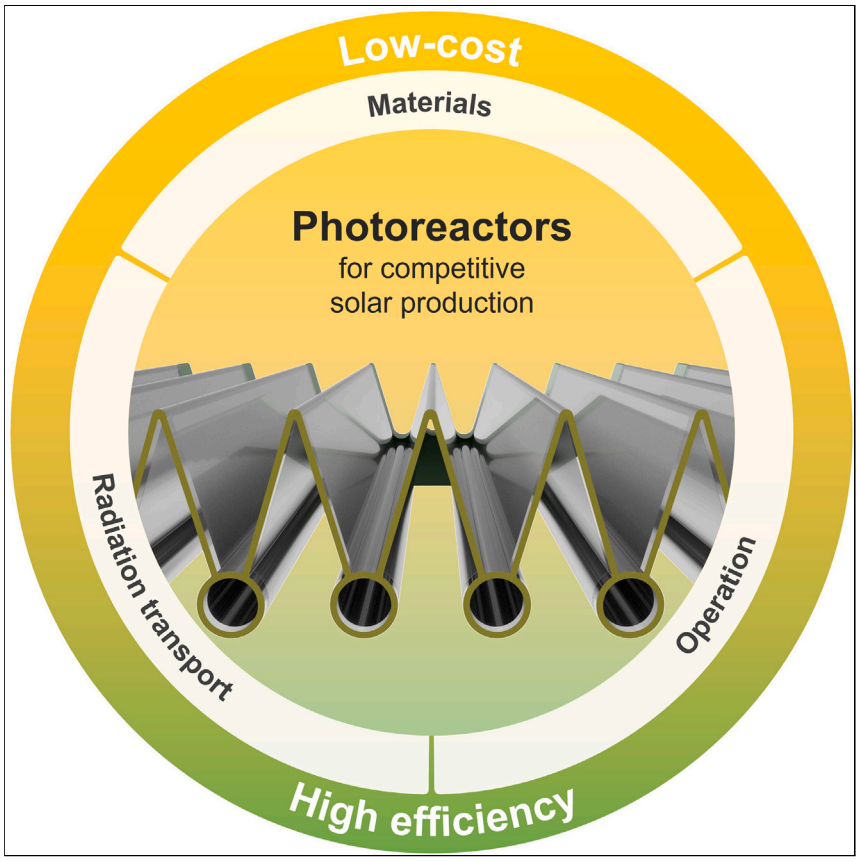

The implementation of solar-driven photosynthesis in a sustainable future world economy requires efficient and low-cost photocatalysts and photoreactors. The manuscript introduces a polymer photoreactor that is especially low-cost in production but can nevertheless ensure a high efficiency of the overall system. The described methodology for photoreactor optimization and a derived design guideline, thereby, facilitate the adaptation of the photoreactor to various photocatalysts. The versatility of this approach contributes to the further development of the dream of solar-produced energy carriers and chemical feedstocks.

Paul Kant, Shengzhi Liang, Michael Rubin, Geoffrey Alan Ozin, Roland Dittmeyer

paul.kant@kit.edu

Highlights

Low-cost photoreactor design concept for solar-driven synthesis

High photocatalytic efficiency throughout the day and year without sun tracking

Concise design guideline for facile photoreactor dimensioning

Kant et al., Joule 7, 1347–1362
June 21, 2023
https://doi.org/10.1016/j.joule.2023.05.006

Joule

CellPress
OPEN ACCESS

Article

Low-cost photoreactors for highly photon/energy-efficient solar-driven synthesis

Paul Kant,[1,*] Shengzhi Liang,[1] Michael Rubin,[2] Geoffrey Alan Ozin,[3] and Roland Dittmeyer[1,2,4]

SUMMARY

Solar-driven photocatalytic processes are an emerging field that inspires hopes and dreams of a sustainable future on planet Earth. Using carbon dioxide and water as feedstocks, photocatalytic processes could deliver the energy and carbon feedstock for the future world economy. However, until today, low achieved photocatalytic efficiencies and high costs of photoreaction technology are hurdles for photocatalytic processes at scale. Within this contribution, a low-cost, milli-to-micro structured, and panel-like photoreactor concept, which is suitable for small-scale decentral and large-scale solar farm applications, is introduced. The key feature is a high achieved photocatalytic efficiency at a low design complexity and system cost. The optical modeling and analysis reveal achievable limits and prevalent loss mechanisms cumulating in a concise design guideline for the proposed photoreactors. The guideline comprehensibly establishes a connection between design parameters and performance metrics at a universal level, thereby providing a basis for adaptation and further development in the field of solar-driven photosynthesis.

INTRODUCTION

Solar-driven photocatalysis is an emerging research field with various envisaged application scenarios.[1–4] In addition to implying a huge carbon dioxide utilization potential, solar-driven photocatalytic conversion of carbon dioxide and water can be an essential building block in pathways that lead toward the goals of the Paris agreement.[5] However, until today, no solar-driven photocatalytic process that uses carbon dioxide and water as feedstock has been implemented at a significant scale. The challenges faced, on the one hand, are low photocatalytic efficiencies,[6,7] typically around 1% from an energetic point of view,[4,8] and, on the other hand, are high costs for the specialized photoreaction technology employed.[6,7,9]

Optimizing a solar-driven photocatalytic process with respect to the achieved photocatalytic efficiency is a multi-discipline task at the interface of material sciences, optics, and chemical engineering.[6,7,10] The keys to success are two core elements. First, it is a materials challenge. The quantum yield of the employed photocatalyst, defined in accordance to the recommendation by the International Union of Pure and Applied Chemistry (IUPAC), Equation 2, must be high in the photon-rich, visible band of the sunlight's spectrum.[11] Second, and of utmost importance, it is a technology challenge. It requires photoreactors that enable high photocatalytic efficiencies, or, in other words, reliably provide operating conditions under which the quantum yield peaks, and, most importantly, ensure a high radiation transport efficiency from the reactor aperture to the reaction volume.[9,12] Non-constant quantum yields that decrease with increasing process intensity, like that revealed, for instance, in

CONTEXT & SCALE

Technologies replacing fossil energy carriers are essential for ways into a sustainable future. Therefore, solar fuels and carbon feedstocks, synthesized from carbon dioxide and water enabled by sunlight, are the subjects of substantial research and development efforts. This work advances the field by introducing a low-cost photoreactor design for solar-driven synthesis. The introduced photoreactors have a low level of complexity, are readily manufacturable via mass fabrication techniques in polymers, and are easy to adapt to diverse photocatalysts. Further, the photoreactors master the two-faceted engineering challenge of (1) guaranteeing operating conditions under which the quantum yield of the photocatalyst peaks and (2) ensuring a high efficiency of radiation transport from the photoreactor aperture to the photocatalyst. The resulting key feature is a photon/energy efficiency that is high throughout the day and year without the need to employ sun tracking.

Kant et al.,[13] thereby, represent a special challenge. To guarantee a high photocatalytic efficiency in such systems, photon absorption must be homogeneous throughout the reaction volume.

Photoreactors for solar-driven synthesis, which are low-cost both in fabrication and operation, (1) would be based on cheap materials,[7,9,11] such as polymers, (2) would, therefore, operate under mild process conditions, (3) would not employ mechanical sun tracking,[9,14] and (4), in the best case, would be modular to be ready for mass production and to adapt to various use cases. In analogy to the cost challenges faced within the field of high-efficiency, multi-junction photovoltaics,[14] the amount of photocatalyst employed in a photoreactor should be minimized by means of smart optical design that increases the use of catalysts to a maximum. A homogeneous illumination of the whole reaction volume, consequently, should be sought.

Herein, a concept for low-cost, high-efficiency, and modular milli-to-micro-structured photoreactors for solar-driven synthesis is introduced. The panel-like photoreactors are intended for use in both small-scale decentral applications (see Figure 1), as well as in solar farms. The design method and base design are applicable to any sunlight-harvesting liquid, gas, or heterogeneous multi-phase photocatalytic system. To ensure comparability with other approaches, however, the design method and the resulting photoreactor are demonstrated experimentally with the established, commercially available, and reliable potassium iron(III) oxalate photocatalytic system. The subsequent analysis reveals theoretical limits for the achievable photocatalytic efficiency within the proposed photoreactors and their dependency on material properties. The detailed loss mechanism analysis that is presented further outlines the design optimization strategies. The derived understanding of achievable limits and loss mechanisms together lead to a concise design guideline for the proposed photoreactors. The guideline connects basic design parameters with performance metrics at a universal level and, thereby, paves the way for various adaptations of the proposed design and optimization approach, even by non-experts in the field.

RESULTS AND DISCUSSION

Optimizing efficiency

The base design is an extrudable array of reaction channels (see the first-level zoomed-in image in Figure 1). The cross section of a single channel comprises a V-shaped concentrator capturing light from various incident directions and guiding it into a tube-like, mirrored cavity, enclosing the reaction volume (see the second-level zoomed-in image in Figure 1). The precise shape of a single concentrator cavity channel is optimized in a way that the achieved UV-vis photocatalytic efficiency (for definition, see experimental procedures and Equation 1) is maximized. The optimization is based on a 3D optical model that employs Monte Carlo ray tracing coupled to a plug flow reactor model that maps the chemical conversion. The optimization, thus, considers the specific optical and reaction engineering properties of the employed reaction system and reactor component materials. The optimization is based on a two-step algorithm, delivering a free-form shape. For details on the proceeding, see the experimental procedures section. For experimental validation, the manufactured optics are included in a single-channel lab photoreactor with standard fluid connectors (see Figure 2). The yellow highlighted cross section of the single channel, thereby, corresponds to the cross section of the imagined production photoreactor presented in Figure 1.

[1]Institute for Micro Process Engineering (IMVT), Karlsruhe Institute of Technology (KIT), Eggenstein-Leopoldshafen, Baden-Württemberg, Hermann-von-Helmholtz-Platz 1, 76344 Eggenstein-Leopoldshafen, Germany

[2]Institute of Catalysis Research and Technology (IKFT), Karlsruhe Institute of Technology (KIT), Eggenstein-Leopoldshafen, Baden-Württemberg, Hermann-von-Helmholtz-Platz 1, 76344 Eggenstein-Leopoldshafen, Germany

[3]Department of Chemistry, University of Toronto (UofT), 80 St. George Street, Toronto, ON M5S 3H6, Canada

[4]Lead contact

*Correspondence: paul.kant@kit.edu

https://doi.org/10.1016/j.joule.2023.05.006

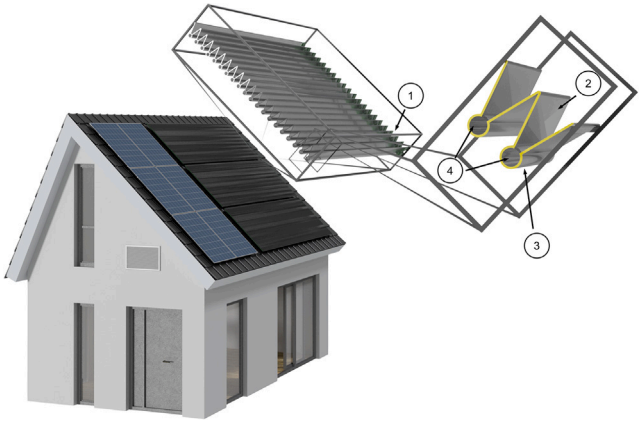

Figure 1. Potential application of the proposed low-cost, high-efficiency photoreactors on the roof top of a low-energy house

The two-level zoom-in highlights the structure of the panel-like photoreactor, which consists of hundreds of parallel reaction channels (see first zoom level). Each reaction channel comprises a V-shaped concentrator and a tube-like cavity, which encloses a reaction volume (see second zoom level showing two channels). Numbering refers to (1) polymer fluid connectors distributing reactor feed and collecting products, (2) transparent polymer optics module with reaction channels, (3) outer reflective coating applied from the bottom only, and (4) individual reaction volumes. A photograph of a 3D-printed prototype is displayed in Figure S15, right.

Showcasing performance

Under collimated simulated solar light perpendicular to the aperture plane (α = β = 0°, angle definitions, see Figure 2), the free-form optimized concentrator cavity channel (CAD model drawing and photograph; see Figure S14) exhibits a UV-vis photocatalytic efficiency of 5.8% for the iron(III)-to-iron(II) photon-induced redox reaction of potassium iron(III) oxalate (see the y-intercept of the bold solid line in Figure 3, left). This number represents a UV-vis photocatalytic efficiency that is more than 4 times higher than that achieved using a simple quartz glass capillary photoreactor, equal to the one used in the free-form optimized photoreactor, but not comprising any optics (see the y-intercept of the dot-dashed line in Figure 3, left). Experimentally determined UV-vis photocatalytic efficiencies agree well with the simulated data, thus underlining the reliability of the conducted simulations and the optimization result (see circles in Figure 3, left). The observed significant performance boost induced by the concentrator cavity channel results from a repeated redirection of scattered and transmitted light toward the reaction volume. Because the redirection of rays is based on reflections, the photoreactors are denoted "reflective multi-pass photoreactors." In analogy to similar approaches in photovoltaics design,[6] the redirection of light toward the reaction volume leads to multiple ray passes that add up to the effective optical path length, thereby increasing the probability of absorption without adding to the physical dimensions of the reaction volume or the photocatalyst mass, respectively. Seen from this perspective, the geometry optimization objective is maximizing the number of ray passes through the reaction volume. At the same time, as a consequence of multiple ray passages, the whole reaction volume is reached by photons, and the use of catalysts is maximized. The achieved peak UV-vis photocatalytic efficiency of 5.8 % might seem unimpressive at first, but it corresponds to approximately 62 % of the material property-determined, theoretically achievable limit (see section "understanding the limits").

Most importantly, the proposed design shows a pronounced tolerance toward the direction of incident light. This characteristic is decisive for any low-cost, solar-driven

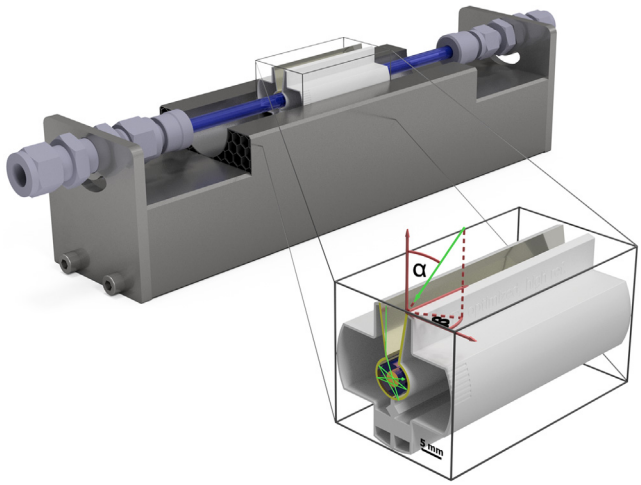

Figure 2. Computer-aided design (CAD) model rendering of the single-channel lab photoreactor employed for the demonstration of the proposed photoreactor concept

The zoomed-in image shows the details of the concentrator cavity channel shape (light gray) and highlights an exemplary ray path (thin green line) of light traveling through the reaction volume (orange) enclosed by a quartz glass capillary (dark blue in the center). The cross-section shape, that both the lab demonstrator and the envisioned production reactor in Figure 1 have in common, is highlighted in yellow. The red polar coordinate system highlights the incidence direction definition by the angles α and β that is used throughout the manuscript. Rotation of the channel optics around the reactor axis allows for an experimental variation of the incidence direction with respect to α under β = 0 ° without moving the light source shining into the reactor aperture from above. For a photograph of the single-channel lab photoreactor, please refer to Figure S15, left.

photocatalytic process.[14] With the proposed concentrator cavity channels statically aligned with an East-West axis and the reactor aperture normal statically oriented toward the sun path at equinox, the achieved UV-vis photocatalytic efficiency is high both throughout the day and the year (Figure 3, right). This critical property allows an application without continuous mechanical sun tracking; therefore, it not only significantly reduces the capital expenditure (CAPEX) and operational expenditure (OPEX)[14] but also paves the way for small-scale decentralized applications on rooftops,[14] with the potential for a broad impact on the energy market.[15] The advantageous incidence direction characteristic of the proposed design is a consequence of the low realized light concentration ratio (see the law of etendue conservation, explained in Smestad et al.[16]) of the channel cross section and the axial extension of the geometry. On a side note, the sun paths during the summer and winter solstices, depicted in Figure 2, right, highlight that the acceptance angle range, with respect to the angle α (under β = 0 °) of a statically, but optimally, oriented channel-like photoreactor, does not need to be higher than ±23.5 ° to be operational throughout the day and year.[14] This design requirement directly results from the obliquity of the ecliptic of 23.5 °.

Literature-standard photoreactors, for instance, tube bundle or panel photoreactors, have higher acceptance angle ranges than the introduced reflective multi-pass photoreactors. Consequently, on the one hand, they perform more homogeneously throughout the year, but, on the other hand, achieve significantly lower photocatalytic efficiencies. Importantly, in an all-year average, the introduced reflective multi-pass photoreactors outperform tube-bundle and panel-like photoreactors (see the supplemental information section on photoreactor benchmarking).

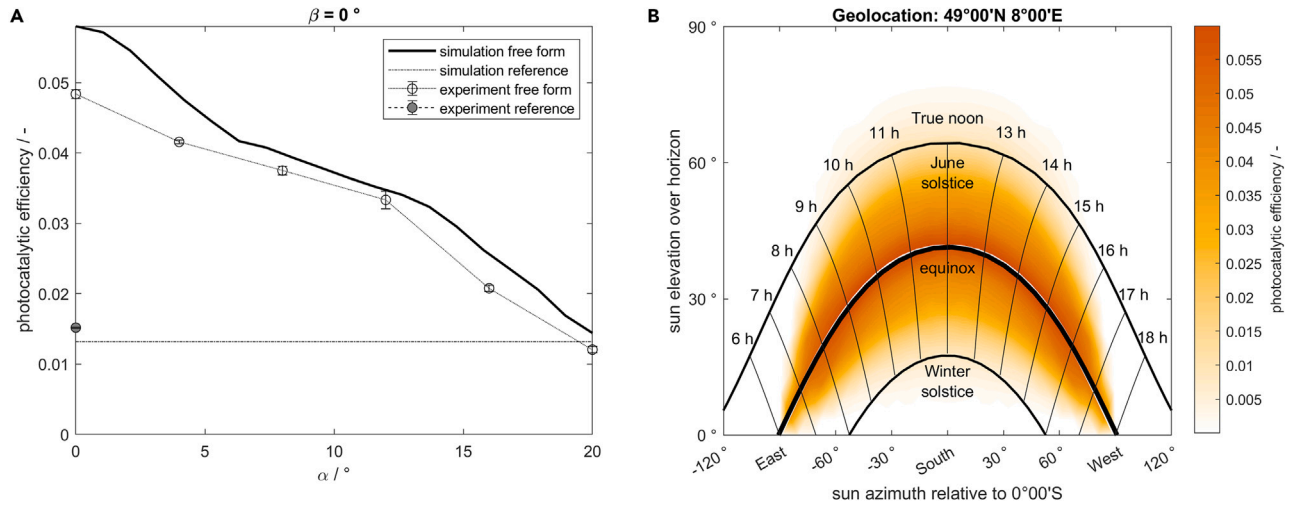

Figure 3. Performance of an optimized reflective multi-pass photoreactor

(Left) Photocatalytic efficiency for the photon-induced decomposition of potassium iron(III) oxalate drawn over the polar incidence angle α under the azimuth incidence angle β = 0 ° (for details on the referred coordinate system, see Figure 2). Simulation data for the free-form optimized shape and the reference quartz glass capillary are presented by a bold solid line and a dot-dashed line, respectively. Experimental data for the free-form optimized shape and the reference quartz glass capillary are presented with empty and filled circles, respectively. Error bars correspond to one standard deviation propagated from the error in the space time yield estimation. (Right) Simulated photocatalytic efficiency of the free-form optimized channel in diurnal and annual variation at 49°00′N 8°00′E (corresponds approximately to Karlsruhe, Germany). The channel is optimally aligned with the sun path. Precisely, it is axially aligned with an east-west axis, and its aperture normal points toward the sun path at equinox. The bold solid lines represent the sun paths on December 21st (Winter solstice), March 21st/September 23rd (equinox), and June 21st (June solstice). Thin solid lines represent isolines of the solar time along the sun paths. Following a selected sun path and paying attention, the color coding gives the diurnal variation of the photocatalytic efficiency at a specific day in the year. Following a solar time, isoline gives the annual variation of the photocatalytic efficiency at a specific solar time. Simulations underlying the graph were varying α and β in a hemisphere assuming an infinite reaction channel length. Sun path calculations are based on the astronomical algorithms by Meeus (for details, see Meeus[26]) and have been conducted with the sun path calculator by the National Oceanic and Atmospheric Administration.

Understanding the limits

Improving the achieved photocatalytic efficiency in reflective multi-pass photoreactors is constrained from two directions. First, the spectral dependency of the quantum yield of the photocatalytic system employed sets an ultimate limit for the achievable efficiency. For the potassium iron(III) oxalate system used in this work, literature data[17] on the quantum yield indicate that only photons with a wavelength less than 550 nm can induce a photoreaction (see the empty circles in Figure 4, right). Only about one third of all UV-vis photons of the solar spectrum fulfill this criterium. Noteworthily, a quantum yield differing from zero is a necessary but not sufficient condition to achieve photocatalytic conversion within a photoreactor. The second necessary, obvious, but non-trivial condition is photon absorption in the reaction volume. The latter is determined by radiation transport processes shaped by the reactor geometry and the optical properties of the employed construction materials.

The efficiency of radiation transport from the reactor aperture to the reaction volume in reflective, multi-pass photoreactors is constrained by inherent absorptive losses that occur when light is traveling through the reactor assembly. Although the concentrator cavity channel walls are silver coated, and the quartz glass tubing is highly transparent, each wall reflection and each pass through the quartz glass tubing reduce the share of the incident photon flux that can be absorbed within the reaction volume. However, there are optimal ray paths on which such parasitic absorption is minimized. These optimal ray paths are characterized by two critical properties. First, optimal ray paths have a long ray path segment length in the reaction volume, which reduces the number of necessary ray passes until full absorption

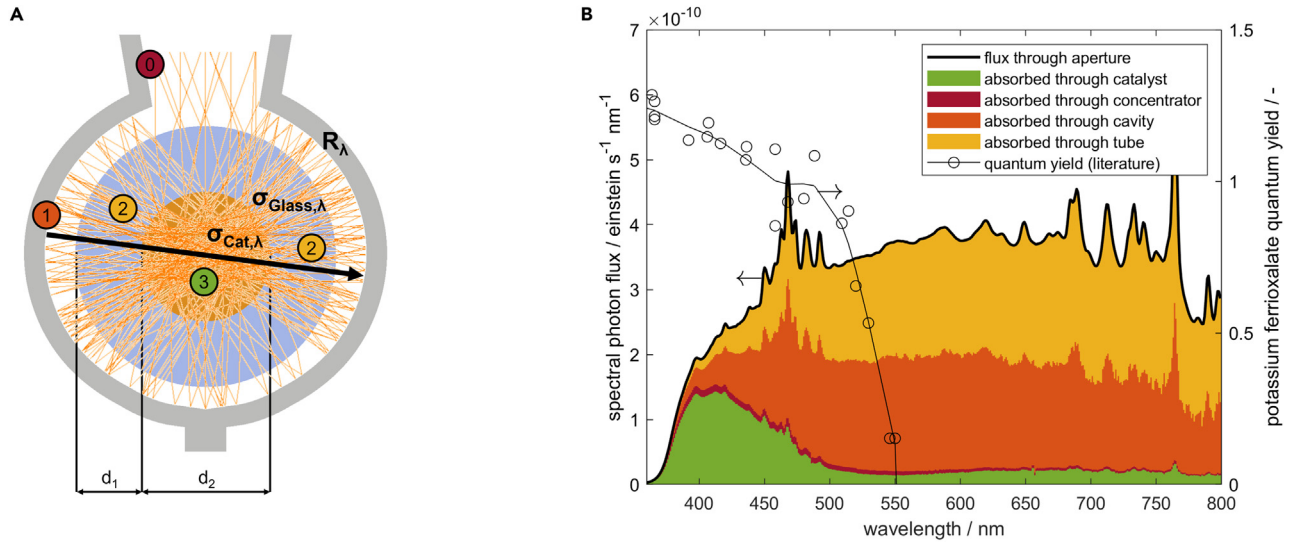

Figure 4. Theoretical limits achievable within reflective multi-pass photoreactors

(Left) Ideal ray path segment (black bold arrow) characterized by minimal inherent parasitic absorption share through concentrator (0), cavity walls (1), and glass (2) and maximum feasible absorption share through the catalyst (3) together with 10 representative ray paths in the free-form optimized concentrator cavity channel with an incidence direction given by $\alpha = \beta = 0°$ (orange). (Right, left axis) Spectral photon flux sent into the reactor aperture (bold solid line) and spectral photon absorption shares (colored areas) derived assuming light traveling only on ideal ray paths in the reactor cross section plane until complete photon absorption. (Right, right axis) Literature data[17] on the quantum yield of the potassium iron(III) oxalate system (empty circles with thin solid line fit). The "solar" spectrum underlying the presentation corresponds to the experimentally determined spectrum of the class ABA solar simulator employed in this work.

of the ray's photons. This reduces the number of cavity wall reflections or parasitic absorption losses on the mirror coating, respectively. Second, ideal ray paths show a high ratio between ray path segment length in the reaction volume and ray path segment length in the surrounding glass. This minimizes the effect of parasitic absorption by the glass. In a circular geometry of reaction zone and surrounding glass, ideal ray paths go through the center of the assembly (Figure 4, left).

Adding up the absorption contributions through the reaction volume in an infinite series of ray passes on ideal ray paths through the assembly allows the estimation of a maximum feasible reaction volume absorption share or a maximum feasible spectral radiation transport efficiency, respectively (green area in Figure 4, right). By analogy, adding up the absorption shares of the cavity wall and quartz glass tubing leads to minimum feasible parasitic absorption shares (yellow and orange areas Figure 4, right). Importantly, the maximum/minimum absorption shares are solely determined by the characteristic dimensions of the reaction volume and glass tubing (d_1 and d_2, Figure 4, left) and the optical properties of the reaction volume and reactor component materials (absorption coefficients of glass and reaction volume $\sigma_{Glass,\lambda}$ and $\sigma_{Cat,\lambda}$, and wall reflectivity R_λ, all being wavelength dependent). For details on the mathematical derivation of the absorption shares and their dependency on geometric and material properties, please refer to the corresponding section of the supplemental information.

The spectral course of the spectral radiation transport efficiency limit in Figure 4, right, reveals the importance of an appropriate choice of materials and characteristic dimensions in reflective multi-pass photoreactors. Just in the band from 450 to 500 nm, in which both the spectral flux through the reactor aperture and the quantum yield are high, the maximum feasible spectral radiation transport efficiency, or

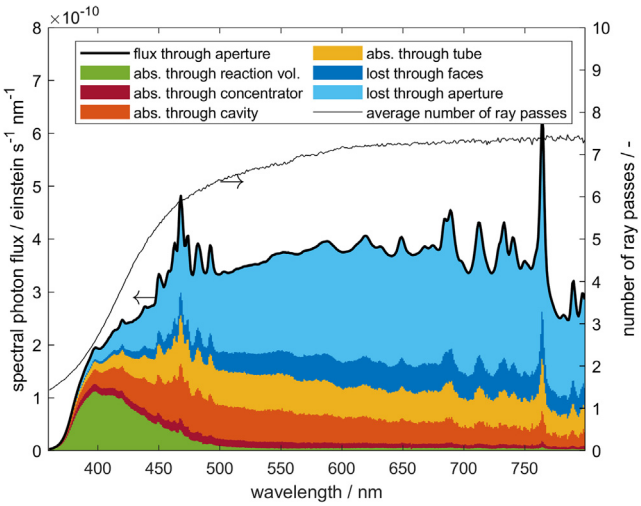

Figure 5. Loss mechanism analysis in reflective multi-pass photoreactors

Spectral photon flux sent into the reactor aperture (bold solid line) together with simulated spectral absorption and loss shares (colored areas) for the free-form optimized concentrator cavity channel (real, non-ideal ray paths!). Blue color represents loss shares over aperture (light blue) and faces (dark blue). Red, orange, and yellow colors represent parasitic absorption shares by the concentrator, cavity, and glass tubing. The thin solid line depicts the registered average number of real, non-ideal ray passes through the reaction volume prior to full photon absorption or loss through aperture or faces. The simulation underlying the depicted data was conducted assuming an incidence direction given by $\alpha = \beta = 0$ °.

the maximum share of absorption by the reaction volume, respectively, is low (green area in Figure 4, right). This system behavior is predominantly triggered by a decrease in the absorption coefficient of the employed potassium iron(III) oxalate solution dropping over 2 orders of magnitude from approximately 109 m^{-1} at 400 nm to 12. 5 and 1. 0 m^{-1} at 450 and 500 nm, respectively (see Figure S8). As a consequence, although the reflectivity of the cavity's coating is higher than 95 % throughout the band from 450 to 500 nm (see material data in Figure S8), absorption by the cavity wall and the quartz glass tubing will dominate the radiation transport problem for wavelengths above 450 nm. Therefore, the maximum achievable UV-vis photocatalytic efficiency in the reported system equals "only" 9.8 %, and the reported achieved 5.8% UV-vis photocatalytic efficiency translates to impressive 62% of what can be achieved in the reported system defined by its characteristic dimensions and employed materials.

Analyzing loss mechanisms

Beyond inherent, unavoidable parasitic absorption losses shaping the achievable limits, real systems depict further losses, explaining the deviations between what can be achieved and what is achieved. These losses are on the one hand absorptive losses induced by non-ideal ray paths with a higher than minimum absorption share of the glass tubing and cavity wall (orange ray paths depicted in Figure 4, left). On the other hand, there are losses induced by rays that leave the concentrator cavity channel after multiple internal reflections prior to full photon absorption. Thus, the losses depicted in Figure 4, right, do not show the full picture of a real system. For the reported free-form concentrator cavity channel, in the optical band above 450 nm, losses through the aperture and faces dominantly contribute to the radiation transport problem (see the blue areas in Figure 5). The number of reaction volume passes that a reflective multi-pass photoreactor can guarantee before a ray is lost through the aperture or over channel faces, thereby becoming an important

characteristic for optimizing the efficiency of a reflective multi-pass photoreactor. The realistically feasible number of reaction volume ray passes in the free-form concentrator cavity channel reported in this work lies just above seven ray passes (see the asymptote of the thin solid line for increasing wavelengths or decreasing system absorption respectively, Figure 5). It is noteworthy that the necessary number of reaction volume ray passes prior to full photon absorption can lie significantly below the number of reaction volume ray passes that a design can guarantee in case the absorption on a single reaction volume ray pass is significant enough. For the free-form concentrator cavity channel, this is maintained in the optical band from the UV up to approximately 450 nm (see the thin solid line in Figure 5).

Design guideline

Considered cumulatively, the discussion of the theoretical limits for the spectral radiation transport efficiency and the analysis of prevalent loss mechanisms in a real reflective multi-pass photoreactor allows for the derivation of a straightforward universal design guideline, supporting the materials selection and the determination of suitable characteristic dimensions in reflective multi-pass photoreactors. The guideline aims for two critical system properties. First, the materials and characteristic dimensions of the cavity, reaction volume, and surrounding glass must be chosen in a way that the achievable spectral radiation transport efficiency is high throughout the relevant optical band. The relevant band is dictated by the solar spectrum and the spectral dependency of the quantum yield in the desired photoreaction, compare Figure 4, right. On a side note, in this regard, the free-form concentrator cavity channel example presented in this work is designed sub-optimally because the achievable radiation transport efficiency limit is low in the band in which the light source irradiance and quantum yield are high (see section "understanding the limits"). Second, the materials and characteristic dimensions must be chosen in such a way that a reasonable number of reaction volume ray passes leads to a significant total share of photon absorption, meaning that the total share of the incident photon flux being absorbed by reactor components is significant. Losses over the aperture and faces such as those described in the section "analyzing loss mechanisms" are minimized under this condition. For the free-form concentrator cavity channel reported in this work, a "reasonable number" corresponds to less than seven ray passes (see Figure 5). At the same time, the number of ray passes necessary to achieve a significant total photon absorption share should not be below two to avoid that there are regions in the reaction volume that are not reached by any light due to the reaction volume shading itself by intense photon absorption. This condition will ensure full catalyst usage, and, thereby, reduce the amount of catalyst employed in the photoreactor to a minimum needed. Further, a minimum number of ray passages ensures that gradients in the intensity of photon absorption in the reaction volume are small. In case the quantum yield decreases with an increasing intensity of photon absorption (for instance, similar to that described in Kant et al.[13]), the control of the intensity of photon absorption is a crucial aspect of a high-efficiency photoreactor.

Figure 6 shows a graphical representation of the mathematics (for details, see the corresponding section of the supplemental information) behind the proposed design guideline. The depicted design map interconnects optical properties and characteristic dimensions of the critical reactor components with the achievable photocatalytic efficiency and the number of ideal ray passes necessary to guarantee the desired total share of photon absorption. For a given Napierian absorbance (assuming Beers law) of the glass tubing (y axis) and a desired design spectral radiation transport efficiency limit (color coding), the depicted lines with constant cavity

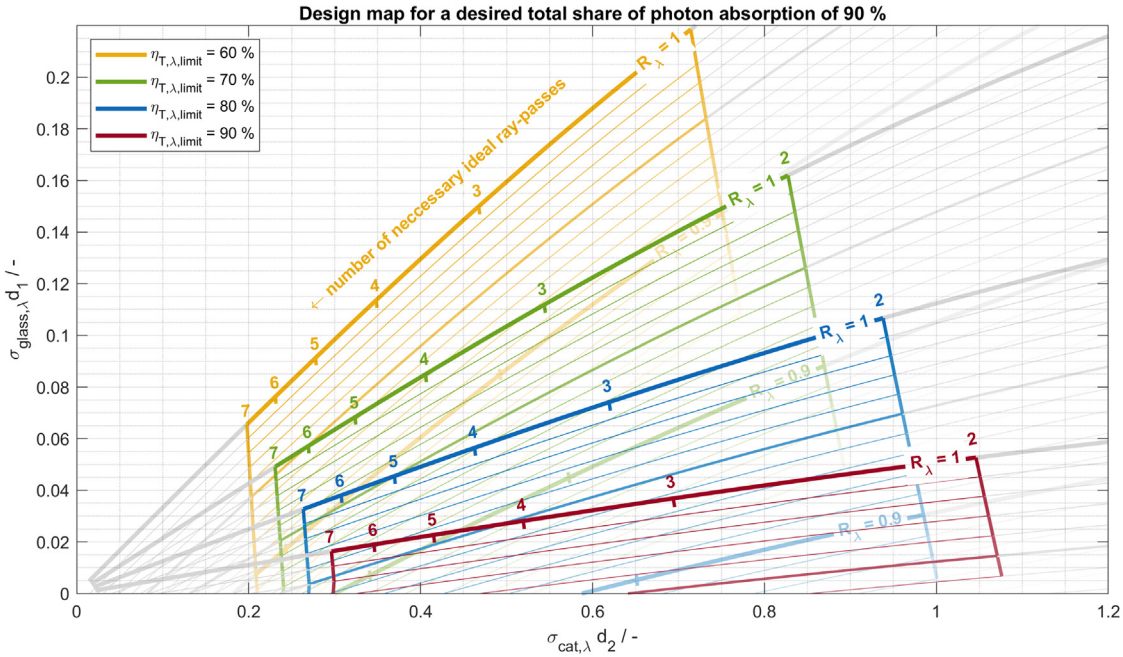

Figure 6. Graphical design map for reflective multi-pass photoreactors

The graph connects the Napierian absorbance of the employed quartz tubing (given by $\sigma_{Glass,\lambda}d_1$, y axis), the reflectivity of the employed cavity wall coating (given by R_λ, light gray and colored lines) and the Napierian absorbance of the reaction volume (given by $\sigma_{cat,\lambda}d_2$, x axis) with the achievable spectral radiation transport efficiency ($\eta_{T,\lambda,limit}$, color coding) and the minimum number of ray passes necessary to ensure the desired total share of photon absorption (ticks along the lines with constant reflectivity). The depicted lines with constant cavity wall reflectivity link a given Napierian absorbance of the glass tubing with the Napierian absorbance of the reaction volume necessary to ensure the desired maximum feasible spectral radiation transport efficiency limit. The four employed colors refer to four different design feasible spectral radiation transport efficiency limits between 60% and 90%, from yellow to green, over blue to dark red. Ticks along the lines of constant cavity wall reflectivity indicate the number of ray passes on ideal ray paths necessary to achieve a total share of photon absorption of 90%. The color highlighting above the gray iso-reflectivity lines depicts the range from two to seven ideal ray passes, which is chosen to meet the number of ray passes that seem feasible within real systems.

wall reflectivity link the given set of reactor component material properties to a Napierian absorbance of the reaction volume (x axis) that is necessary to ensure the desired total share of photon absorption and the targeted spectral radiation transport efficiency at the same time. From the necessary Napierian absorbance of the reaction volume, the suitable characteristic dimension of the reaction volume, in the case the absorption coefficient of the reaction volume is known, can be derived. In case the characteristic dimensions of the reaction volume are fixed, the needed catalyst absorption coefficient, or catalyst concentration, can be derived. Finally, the ticks along the lines with constant cavity wall reflectivity in Figure 6 allow an estimation of the minimum number of ideal ray passes that are needed to ensure the desired total share of photon absorption. As outlined in detail, this minimum number of ray passes must be ensured by the optics around the reaction volume; thereby, it sets the requirements for the geometry of the optical components of the photoreactor to be designed. As shown above, sophisticated Monte Carlo ray tracing simulations coupled with geometry optimization tools are a promising way to address this creative challenge to find such geometries.

Estimating costs and revenues

Implementing new technologies requires economically extremely attractive approaches. Both return on investment and interest rates must be high, especially for non-established technologies that apparently bring along a high risk.

For the introduced reflective multi-pass photoreactors, costs are extremely low. Being made from three polymer parts only (two fluid connectors and one optics module, see Figure 1), all produced via established mass-manufacturing techniques, the material cost of the reactor components is estimated to be in the range of 9.4 \$ m^{-2} (see preliminary feasibility study in the supplemental information). Assumed materials are, thereby, polycarbonate for the optics module and polyethylene for the fluid connectors. The reflective layer is assumed to be a sputtered aluminum layer. Including a catalyst worth 1 million \$ per ton, the material cost estimate of the photoreactor system increases to roughly 22 \$ m^{-2}.

Assuming a water splitting photocatalyst with a quantum yield equal to unity in the optical band from 360 to 450 nm, the annual production of such a photoreactor can be estimated to be roughly 870 mol a^{-1} hydrogen plus 435 mol a^{-1} oxygen, which results an annual revenue of roughly 7.5 \$ m^{-2} a^{-1}. A linear return on investment and a 10-year interest rate would, consequently, be as high as 34 % and 24 %, respectively. Those are promising numbers. Noteworthily, they do not include the manufacturing cost of reactor components, the plant costs, or the cost of operation and therefore are only rough estimates. For further discussion, see corresponding section of the supplemental information. On a side note, the assumed photocatalyst is an optimistic but not unrealistic assumption. Both water splitting photocatalysts that show a quantum yield close to unity[2] and water splitting photocatalysts that operate with photons in the blue band of visible light[18] are already reported.

Conclusions

Low-cost and high-efficiency photoreactors are the essential keys to the success of solar-driven photosynthesis. Within this work, a concept for modular, milli-to-micro structured photoreactors, which ensure sufficiently high photocatalytic efficiency without the need for sun tracking and with low cost in fabrication and operation, is introduced. The proposed design guideline for the general dimensioning of reflective multi-pass photoreactors takes into consideration all major design parameters and facilitates the adaptation and further development of the design approach by researchers and engineers in the field of photocatalysis and photoreaction engineering. Although the introduced design and optimization approaches are showcased with an exemplary photocatalytic system, the strength of the approach and optimization strategy is its adaptability to any liquid phase or gas phase that is a heterogeneously catalyzed photocatalytic system. However, future work must address the extension of the design guideline to photocatalysts that scatter light in addition to absorbing it.

Operated with a low-temperature-active photocatalyst, the envisaged micro-channel arrays could be mass-manufactured through extrusion of polymers with subsequent sputtering of a thin aluminum layer, ensuring high reflectivity of the concentrator and cavity walls, simultaneously, at low cost of the channel array itself. The preliminary feasibility study reveals a high economic potential because of extremely low cost of the photoreactors. Optical dilution of the reaction volume through impregnation of heterogeneous catalysts on a transparent catalyst support, such as a silica aerogel (for an example, see Kant et al.[13]), would allow the precise tuning of the optical properties of the reaction volume, which, as outlined in detail, are one corner stone in the complex system determining the achieved photocatalytic efficiency.

Further optimization of the photoreactor should address the manufacturing of the key components in polymers and the consideration of real-world aspects such as aging of polymers and optical coatings, as well as challenges such as dust accumulation

in the rather complicated surface of the photoreactor aperture. A cover being extruded with the optic module could represent one approach to address the latter challenge. Furthermore, to achieve higher photocatalytic efficiencies during the summer and winter solstices, the acceptance angle range could be increased by modifying the simple narrowing gap concentrator. For example, it could be achieved through a free-from optimization or by replacing it with a compound parabolic concentrator with a similar concentration ratio.

Paving the way toward the large-scale implementation of solar-driven photocatalytic processes by allowing low-cost fabrication and operation and high efficiency at the same time, the introduced photoreactor design and approach is a significant step. Nevertheless, being only one piece of the puzzle in the bigger picture, a long way toward a reasonable humanity living in sustainable societies remains to be mastered.

EXPERIMENTAL PROCEDURES

Resource availability

Lead contact

Further information and requests for resources and materials should be directed to and will be fulfilled by the lead contact, Roland Dittmeyer (roland.dittmeyer@kit.edu).

Materials availability

This study did not generate new, unique materials.

Data and code availability

The employed Monte Carlo ray tracing environment, the code of the optimization algorithm, the code generating the graphical design guideline, and the experimental data presented in the manuscript are available under https://doi.org/10.5445/IR/1000158287.[19] The Monte Carlo ray tracing environment is used in multiple projects and has been published before (see Kant[20]). Further, a supplemental information provided with the contribution gives detailed information on the following: (1) the simplified optical model underlying the considerations regarding achievable limits and the reactor design guideline, (2) numerical optimization tools developed and employed in this work, (3) measured/assumed light source and material properties, (4) validation data for the developed and employed Monte Carlo ray tracing environment, (5) additional imaging of the photoreactors, (6) a detailed application example of the proposed design guideline, (7) a section reporting on the benchmarking of the introduced photoreactors, and, lastly, (8) the preliminary feasibility study.

Radiation transport modeling

In analogy to literature-reported work,[20,21] the polychromatic optical simulations were conducted in an in-house developed MATLAB-based Monte Carlo ray tracing optical simulation environment. The environment maps specular and/or diffuse reflection on walls, partial reflection, and refraction on phase boundaries and volume absorption and scattering. Volume scattering is assumed to be isotropic. Reflecting surfaces are mapped as partially specular and partially diffuse with defined specular share. The implementation is validated against various literature models for radiation transport (see Figure S10). Polychromatic results are derived through retracing of pre-calculated ray paths that are derived in a simulation assuming no absorption of any component in the reaction channel. The retracing procedure reduces the need for the computation time determining ray object intersection searches and yields the same simulation results if reflection characteristics, scattering, and refraction are no strong functions of the wavelength (Figure S11).

The material datasets assumed in the simulations for all reactor components are depicted in Figure S8. The light sent into the reactor aperture was modeled via a planar ray source in the reactor aperture with a divergence half angle of 0.7° and a primary orientation given by the incidence angles α and β (definition, see Figure 2). The divergence half angle of 0.7 ° equals the manufacturer indication on the degree of collimation of the employed solar simulator.

To reduce the computational effort in the optimization runs and the calculation of the incidence direction characteristic, Figure 2, right, the number of rays needed for convergence in the objective variable was derived in an exemplary simulation case previously to the optimization (Figure S12, left). A number of 50,000 rays in each simulated optical band were found to be sufficient to map the space time yield/photocatalytic efficiency of the photoreactors with a relative standard deviation in repeat simulations of less than 0.5%. The required optical band width of the polychromatic simulations in the optimization runs was determined in a band width study previously to the optimization (Figure S12, right). A band width of 18.75 nm (8 bands between 360 and 550 nm) was found to be sufficient with deviation of less than 5 % relative to the case with a band width of 4.68 nm. The optical band width in the simulations underlying the loss mechanism analysis, Figure 5, was 1 nm to yield maximum resolution and ensure comparability to the calculations regarding the spectral radiation transport efficiency limit in section "understanding the limits".

Reactor modeling

In the reported simulations, the photocatalytic efficiency, definition Equation 1, is derived via the following photoreactor design equation: the reaction volume (V) and wavelength (λ) integral over the product of local spectral photon absorption rate ($L^a_{p,\lambda}$) and the quantum yield (Φ, definition Equation 2) related to the incident photon flux in the reactor aperture ($q_{n,p}$), Equation 3. The definitions of photocatalytic efficiency and quantum yield are in line with the IUPAC recommendations.[22]

$$\eta_{p,system} := \frac{\#\ of\ production\ events}{\#\ of\ incident\ photons\ in\ aperture\ (integral)} \quad \text{Equation 1}$$

$$\Phi := \frac{\#\ of\ production\ events}{\#\ of\ photons\ absorbed\ by\ catalyst\ at\ specific\ wavelength} \quad \text{Equation 2}$$

$$\eta_{p,system} = \frac{\int\int L^a_{p,\lambda}\Phi dV d\lambda}{q_{n,p}} \quad \text{Equation 3}$$

The incident photon flux is derived from the area (A) and wavelength integral of the spectral photon irradiance ($E_{p,\lambda}$) in the reactor aperture (Equation 4). The selected wavelength range for the integration goes from 360 to 800 nm. This range equals the measurement range of the spectrometer employed for the light source characterization.

$$q_{n,p} = \int\int E_{p,\lambda} d\lambda dA \quad \text{Equation 4}$$

Because, if the operating conditions are chosen properly,[23] the quantum yield of the potassium ferrioxalate system is fairly independent of concentration of the reactants and the local spectral photon absorption rate, for the evaluation of Equation 3, it is sufficient to know a volume average spectral photon absorption rate ($\overline{L^a_{p,\lambda}}$), which can be expressed as the product of the spectral incident photon flux in the reactor aperture ($q_{p,\lambda}$) and a spectral radiation transport efficiency in the photoreactor ($\eta_{T,\lambda}$) divided by the reaction volume (see Equation 5). The spectral radiation transport

efficiency represents the share of photons at a defined wavelength sent into the reactor aperture that finally is absorbed in the reaction volume. In the Monte Carlo ray tracing simulations, it is derived from absorption ray counts (Equation 6).

$$\eta_{p,system} = \frac{\int \overline{L^{a}_{p,\lambda}} V \Phi d\lambda}{q_{n,p}} = \frac{\int q_{p,\lambda}\, \eta_{T,\lambda} \Phi d\lambda}{q_{n,p}} \quad \text{Equation 5}$$

$$\eta_{T,\lambda} = \frac{\int L^{a}_{p,\lambda} dV}{q_{p,\lambda}} = \frac{N_{rays,abs}}{N_{rays,simulated}} \quad \text{Equation 6}$$

The theoretical limit for the photocatalytic efficiency reported in the section "understanding the limits" is derived via integration of Equation 5, assuming $\eta_{T,\lambda}$ equaled $\eta_{T,\lambda,limit}$ (details on the mathematical modeling of $\eta_{T,\lambda,limit}$, see supplemental information).

Geometry optimization

The geometry optimization is conducted in two consecutive steps. In the first step, a parameterized geometry comprising a circular cavity and a simple-as-possible narrowing gap concentrator is optimized regarding the cavity diameter and the cavity entry slit width. For definitions of the geometry parameter definitions, see Figure S13. The optimization of the parameterized geometry was conducted using the surrogate-based optimization tool from the MATLAB Global Optimization Toolbox.

In the second optimization step, the geometry from the first step is further improved by inducing free-form deformations in the geometry of the first optimization step. The employed free-form optimization is based on an in-house developed "hammering" algorithm. For details on the proceeding, see the corresponding section of the supplemental information, especially Figure S3.

Reactor fabrication

The optics were 3D-printed in 316L stainless steel via laser induced powder bed fusion in a Realizer SLM 125 printer and galvanically coated with silver for higher reflectivity in the UV-vis band. Silver coating was conducted by C. Jentner in Pforzheim. A high specular share in the reflection was ensured by polishing of the 3D-printed optical surfaces before silver coating via micro milling using a Kern HSPC milling machine and subsequent 4-step graded manual polishing with DIACOMPLETE Poly polycrystalline diamond suspensions from QATM with particle sizes of 6, 3, 1, and 0.25 μm.

Optical property determination

The absorption coefficient of the 2 mM ferrioxalate solution was derived from UV-vis transmission measurements with an Agilent 8453 UV-vis spectrometer. The layer thickness of the employed quartz glass cuvette was 10 mm. The evaluation was assuming Lambert Beer's law for ray attenuation. The quantum yield of the photodecomposition reaction of potassium iron(III) oxalate was taken from literature data.[17] The refractive index of the solution was assumed to equal the refractive index of pure water taken from the literature.[24]

The refractive index and absorption coefficient of the quartz glass capillary were derived from manufacturer data on UV-vis transmission of three samples with thicknesses of 1, 1.5, and 2 mm. The evaluation was based on the assumptions of perpendicular irradiation with a fully collimated ray, Lambert Beer's law for ray attenuation in the glass, and a reflectivity of the two subsequent phase boundaries derived from Fresnel equations.

The reflectivity of the silver channel coating was derived on a planar test piece processed equally to the optics and using a Perkin Elmer Lambda 1050 UV-vis spectrometer equipped with an integrating sphere assembly. The specular share of the reflectivity of the silver coating was estimated from reflectivity measurements with and without a specular trap. For the reflection standard, a Zenith Polymer diffuse reflection standard calibrated with a reference from the Physikalisch Technische Bundesanstalt (PTB) from Sphere Optics was employed.

All determined and assumed material data is presented in Figure S8.

Solar simulator characterization

The employed SS1.6KXeFR-B class ABA (for definition of class ABA, see ASTM standard E927-10) solar simulator from Sciencetech produced collimated radiation closely matching an AMD1.5D reference spectrum regarding the spectral distribution (see Figure S7) and spatial inhomogeneity (<5% spatial inhomogeneity in the target plane). The intensity could be dimmed with neutral density mesh filters and the power setting of the short arc. For meaningful evaluation and assessment, the spectrum of the light source was recorded in the experiment area under experiment conditions using a calibrated CAS 140 CT spectrometer from Instrument Systems equipped with an EOP 120 diffusor from Instrument Systems (see Figure S7).

Potassium iron(III) oxalate experiments

Potassium iron-(III)-oxalate is well known to undergo photon-absorption-induced reduction to potassium iron-(II)-oxalate (see Equation 7). It therefore is commonly used in chemical actinometry. There are different established methods for the determination of the conversion.

$$2\left[Fe(C_2O_4)_3\right]^{3-} \xrightarrow{h\nu} 2\left[Fe(C_2O_4)_2\right]^{2-} + C_2O_4^{2-} + 2CO_2 \qquad \text{Equation 7}$$

The experimental methods applied are adopted from the work of Lehóczki et al.[25] For the potassium iron(III) oxalate photon-induced reduction experiments, 2 mM potassium iron(III) oxalate solution (0.4913 g in 0.5 L 0.05 M sulfuric acid) was pumped through the illuminated photoreactor using a HITEC ZANG SyrDosTM tandem syringe pump. To vary the space time, the flow rates were varied from 2.0 mL/min over 2.6 to 3.7 mL/min. The flow rate range was chosen in a way that ferrioxalate conversion was below 11% for all operating points. The reactor aperture was placed in the solar simulator target plane. Incident angles were varied from 0° to 20° (4° steps) via a rotation of the optics around the quartz glass capillary. Liquid samples were taken and stored in the dark for maximum 12 h before further processing. Stationarity of each operating point was checked before sampling with an online Ocean Optics USB4000 UV-vis spectrometer equipped with a FIA-Z-SMA-ULM flow cell from Ocean Optics measuring the potassium iron(III) oxalate absorbance at 375 nm and hence giving an online estimation of the actinometer conversion.

The conversion of the potassium iron(III) oxalate underlying the reported photocatalytic efficiencies was derived in an iron-(II) 1,10-phenanthroline assay. 8 mL of the liquid sample was mixed with 3 mL of 1,10-phenantroline solution (0.1 g in 100 mL of deionized water), 4 mL of sodium acetate buffer solution (1 M sodium acetate in deionized water mixed with 0.5 M sulfuric acid in a volume ratio of 100:63), and 5 mL of deionized water. After 30 min of color development, the absorbance of the resulting solution at 510 nm was determined with an Agilent 8453 UV-vis spectrometer. The assumed molar attenuation coefficient linking the measured absorbance at 510 nm to the iron-(II) concentration in the sample was 1,111.9 m^2/mol. This value was derived via a calibration with

Mohr's salt solutions and found to be in good agreement with literature data.[17] For details on the calibration data, see Figure S9.

The potassium iron(III) oxalate space time yield was derived from the slope of a plot of the measured iron-(II) concentration over the space time. The reported standard errors are the standard errors from the slope estimation propagated to the photocatalytic efficiency. The photocatalytic efficiency of the system was derived from the space time yield multiplied by the reaction volume and related to the incidence photon flux in the reactor aperture in the UV-vis band (from 350 to 800 nm).

SUPPLEMENTAL INFORMATION

Supplemental information can be found online at https://doi.org/10.1016/j.joule.2023.05.006.

ACKNOWLEDGMENTS

The authors acknowledge the financial support by the Helmholtz Association of German Research Centres within the Helmholtz-Program "MTET: Materials and Technologies for the Energy Transition," Topic 3: "Chemical Energy Carriers." The authors thank Tino Weiß and Klaus Trampert (Light Technology Institute, LTI, Karlsruhe Institute of Technology, KIT) for their support with the light source emission spectrum characterization and fruitful discussion on the experiment setup. Special thanks go to Denis Scherhaufer (Institute for Micro Process Engineering, IMVT, Karlsruhe Institute of Technology, KIT) for the high accuracy ultra-milling of optical surfaces on 3D-printed parts and Manfred Kraut (Institute for Micro Process Engineering, IMVT, Karlsruhe Institute of Technology, KIT) for his remarks on the considerations regarding the theoretical limit of the spectral radiation transport efficiency. The authors thank Qihao Jin (Light Technology Institute, LTI, Karlsruhe Institute of Technology, KIT) for discussion regarding the determination of optical properties of optical silver coatings and support with UV-vis reflectance measurements. Furthermore, thanks go to C. Jentner GmbH for friendly support and excellent fabrication of silver coatings on stainless steel parts and QSIL GmbH for the supply of quartz glass capillaries and their support with the determination of optical properties of Ilmasil PN quartz glass.

AUTHOR CONTRIBUTIONS

P.K. developed and wrote the software: the MATLAB-based Monte Carlo ray tracer and the free-form hammering geometry optimization algorithm. P.K. developed methodology: the basic design idea and validation strategy via photon-induced reduction of potassium iron(III) oxalate. S.L. led the experimental investigations. P.K. led the simulative investigation. M.R. setup and performed the preliminary feasibility investigation. P.K. and M.R. derived all visualizations. P.K., S.L., and M.R. wrote the article and led review and editing. P.K., M.R., G.A.O., and R.D. conceptualized the work. M.R., G.A.O., and R.D. supervised and supported the work with persistent and fruitful discussion, feedback on content and figures, and substantial support in the writing phase.

DECLARATION OF INTERESTS

As competing financial interest, the authors declare a pending patent application by the Karlsruhe Institute of Technology addressing the photoreactor design subject to the manuscript. The listed inventors are P.K., G.A.O., M.R., and R.D.

INCLUSION AND DIVERSITY

One or more of the authors of this paper self-identifies as an underrepresented ethnic minority in their field of research or within their geographical location. We avoided "helicopter science" practices by including the participating local contributors from the region where we conducted the research as authors on the paper. We support inclusive, diverse, and equitable conduct of research.

Received: November 22, 2022
Revised: March 31, 2023
Accepted: May 8, 2023
Published: June 2, 2023

REFERENCES

1. Ahmed, S.N., and Haider, W. (2018). Heterogeneous photocatalysis and its potential applications in water and wastewater treatment: a review. Nanotechnology *29*, 342001. https://doi.org/10.1088/1361-6528/aac6ea.

2. Takata, T., Jiang, J., Sakata, Y., Nakabayashi, M., Shibata, N., Nandal, V., Seki, K., Hisatomi, T., and Domen, K. (2020). Photocatalytic water splitting with a quantum efficiency of almost unity. Nature *581*, 411–414. https://doi.org/10.1038/s41586-020-2278-9.

3. Uekert, T., Pichler, C.M., Schubert, T., and Reisner, E. (2021). Solar-driven reforming of solid waste for a sustainable future. Nat. Sustain. *4*, 383–391. https://doi.org/10.1038/s41893-020-00650-x.

4. Schäppi, R., Rutz, D., Dähler, F., Muroyama, A., Haueter, P., Lilliestam, J., Patt, A., Furler, P., and Steinfeld, A. (2022). Drop-in fuels from sunlight and air. Nature *601*, 63–68. https://doi.org/10.1038/s41586-021-04174-y.

5. UNFCC (2015). The Paris Agreement (United Nations).

6. Wang, Q., Pornrungroj, C., Linley, S., and Reisner, E. (2022). Strategies to improve light utilization in solar fuel synthesis. Nat. Energy *7*, 13–24. https://doi.org/10.1038/s41560-021-00919-1.

7. Pinaud, B.A., Benck, J.D., Seitz, L.C., Forman, A.J., Chen, Z., Deutsch, T.G., James, B.D., Baum, K.N., Baum, G.N., Ardo, S., et al. (2013). Technical and economic feasibility of centralized facilities for solar hydrogen production via photocatalysis and photoelectrochemistry. Energy Environ. Sci. *6*, 1983–2002. https://doi.org/10.1039/c3ee40831k.

8. Nishiyama, H., Yamada, T., Nakabayashi, M., Maehara, Y., Yamaguchi, M., Kuromiya, Y., Nagatsuma, Y., Tokudome, H., Akiyama, S., Watanabe, T., et al. (2021). Photocatalytic solar hydrogen production from water on a 100-m2 scale. Nature *598*, 304–307. https://doi.org/10.1038/s41586-021-03907-3.

9. Braham, R.J., and Harris, A.T. (2009). Review of major design and scale-up considerations for solar photocatalytic reactors. Ind. Eng. Chem. Res. *48*, 8890–8905. https://doi.org/10.1021/ie900859z.

10. Dong, Y., Duchesne, P., Mohan, A., Ghuman, K.K., Kant, P., Hurtado, L., Ulmer, U., Loh, J.Y.Y., Tountas, A.A., Wang, L., et al. (2020). Shining light on CO2: from materials discovery to photocatalyst, photoreactor and process engineering. Chem. Soc. Rev. *49*, 5641–6114. https://doi.org/10.1039/d0cs00597e.

11. Fabian, D.M., Hu, S., Singh, N., Houle, F.A., Hisatomi, T., Domen, K., Osterloh, F.E., and Ardo, S. (2015). Particle suspension reactors and materials for solar-driven water splitting. Energy Environ. Sci. *8*, 2825–2850. https://doi.org/10.1039/C5EE01434D.

12. Bala Chandran, R., Breen, S., Shao, Y., Ardo, S., and Weber, A.Z. (2018). Evaluating particle-suspension reactor designs for Z-scheme solar water splitting via transport and kinetic modeling. Energy Environ. Sci. *11*, 115–135. https://doi.org/10.1039/C7EE01360D.

13. Kant, P., Trinkies, L., Gensior, N., Domenik, F., Michael, R., Geoffrey Alan, O., and Roland, D. (2023). Isophotonic photoreactor for the precise determination of quantum yields in gas, liquid, and multi-phase photoreactions. Chem. Eng. J. *452*, 139204. https://doi.org/10.1016/j.cej.2022.139204.

14. Apostoleris, H., Stefancich, M., and Chiesa, M. (2016). Tracking-integrated systems for concentrating photovoltaics. Nat. Energy *1*, 16018. https://doi.org/10.1038/nenergy.2016.18.

15. Dittmeyer, R., Klumpp, M., Kant, P., and Ozin, G. (2019). Crowd oil not crude oil. Nat. Commun. *10*, 1818. https://doi.org/10.1038/s41467-019-09685-x.

16. Smestad, G., Ries, H., Winston, R., and Yablonovitch, E. (1990). The thermodynamic limits of light concentrators. Sol. Energy Mater. *21*, 99–111. https://doi.org/10.1016/0165-1633(90)90047-5.

17. Montalti, M., Credi, A., Prodi, L., Gandolfi, M.T., Michl, J., and Balzani, V. (2020). Handbook of Photochemistry (CRC/Taylor & Francis).

18. Wang, Q., Hisatomi, T., Jia, Q., Tokudome, H., Zhong, M., Wang, C., Pan, Z., Takata, T., Nakabayashi, M., Shibata, N., et al. (2016). Scalable water splitting on particulate photocatalyst sheets with a solar-to-hydrogen energy conversion efficiency exceeding 1. Nat. Mater. *15*, 611–615. https://doi.org/10.1038/nmat4589.

19. Kant, P., Shengzhi, L., Michael, R., and Roland, D. (2023). Low-cost photoreactors for highly photon/energy-efficient solar-driven synthesis: code, simulation data, and experimental data. KITopenData. https://doi.org/10.5445/IR/1000158287.

20. Kant, P. (2022). phoRex & QY photoreactor - Monte Carlo ray tracing in MATLAB® & quantum yield measurements. KITopenData. https://doi.org/10.5445/IR/1000150817.

21. Akach, J., Kabuba, J., and Ochieng, A. (2020). Simulation of the light distribution in a solar photocatalytic bubble column reactor using the Monte Carlo method. Ind. Eng. Chem. Res. *59*, 17708–17719. https://doi.org/10.1021/acs.iecr.0c02124.

22. Braslavsky, S.E., Braun, A.M., Cassano, A.E., Emeline, A.V., Litter, M.I., Palmisano, L., Parmon, V.N., and Serpone, N. (2011). Glossary of terms used in photocatalysis and radiation catalysis (IUPAC Recommendations 2011). Pure Appl. Chem. *83*, 931–1014. https://doi.org/10.1351/PAC-REC-09-09-36.

23. Wriedt, B., and Ziegenbalg, D. (2021). Application limits of the ferrioxalate actinometer. ChemPhotoChem *5*, 947–956. https://doi.org/10.1002/cptc.202100122.

24. Hale, G.M., and Querry, M.R. (1973). Optical Constants of Water in the 200-nm to 200-mum Wavelength Region. Appl. Opt. *12*, 555–563. https://doi.org/10.1364/AO.12.000555.

25. Lehóczki, T., Józsa, É., and Ősz, K. (2013). Ferrioxalate actinometry with online spectrophotometric detection. J. Photochem. Photobiol. A *251*, 63–68. https://doi.org/10.1016/j.jphotochem.2012.10.005.

26. Meeus, J. (1998). Astronomical Algorithms (Willmann-Bell).